Nanoscale

PAPER

View Article Online
View Journal | View Issue

Cite this: *Nanoscale*, 2021, **13**, 8966

Reversible engineering of spin–orbit splitting in monolayer MoS_2 *via* laser irradiation under controlled gas atmospheres†

Xilong Liang,[a,b] Chengbing Qin, *[a,b] Yan Gao,[a,b,c] Shuangping Han,[a,b] Guofeng Zhang, [a,b] Ruiyun Chen,[a,b] Jianyong Hu,[a,b] Liantuan Xiao*[a,b] and Suotang Jia[a,b]

Monolayer transition metal dichalcogenides, manifesting strong spin–orbit coupling combined with broken inversion symmetry, lead to coupling of spin and valley degrees of freedom. These unique features make them highly interesting for potential spintronic and valleytronic applications. However, engineering spin–orbit coupling at room temperature as demanded after device fabrication is still a great challenge for their practical applications. Here we reversibly engineer the spin–orbit coupling of monolayer MoS_2 by laser irradiation under controlled gas environments, where the spin–orbit splitting has been effectively regulated within 140 meV to 200 meV. Furthermore, the photoluminescence intensity of the B exciton can be reversibly manipulated over 2 orders of magnitude. We attribute the engineering of spin–orbit splitting to the reduction of binding energy combined with band renormalization, originating from the enhanced absorption coefficient of monolayer MoS_2 under inert gases and subsequently the significantly boosted carrier concentrations. Reflectance contrast spectra during the engineering stages provide unambiguous proof to support our interpretation. Our approach offers a new avenue to actively control the spin–orbit splitting in transition metal dichalcogenide materials at room temperature and paves the way for designing innovative spintronic devices.

Received 3rd January 2021,
Accepted 28th March 2021

DOI: 10.1039/d1nr00019e

rsc.li/nanoscale

1. Introduction

Spin–orbit coupling (SOC), the relativistic interaction between the spin and momentum degrees of freedom of electrons,[1] has attracted tremendous attention both for its interesting fundamental physics and potential applications in next-generation devices.[2–4] Essentially, SOC plays a crucial role in condensed-matter physics and accounts for a broad range of fascinating phenomena, such as spin Hall effects,[5,6] topological insulation,[7,8] and Majorana and Weyl fermions.[9,10] On the other side, this interaction also provides a route towards manipulating electron spins and thus lies at the core of spintronics.[11,12] According to the symmetry dependence, two alternative mechanisms are responsible for the origin of spin–orbit coupling. For the symmetry-independent case, SOC originates from the spin–orbit interaction in atomic orbitals and thus exists in almost all physical systems.[13] Nonetheless, the symmetry-dependent SOC is only present in crystal structures with broken inversion symmetry, which can be further subdivided into two different types, namely Dresselhaus and Rashba SOC, related to different sources of the electric field asymmetry.[14] The Dresselhaus effect is caused by bulk-induced asymmetry (surviving in the materials without any inversion centers), while the Rashba term is originating from the surface- or interface-induced asymmetry (occurring in the systems with broken out-of-plane mirror symmetry).[15] Generally, these two types of SOC naturally coexist and act on the electron spin as an effective magnetic field.[16] Despite the encouraging progress on the generation and manipulation of SOC in many physical systems (including ultra-cold atoms,[17] quantum wells,[18] nanowires,[19] and organic semiconductors[6]), however, exploring practical spintronic devices at room temperature still has proven difficult due to their modest spin–orbit interaction. To this end, physical systems with enhanced SOC are highly desirable.[20]

[a]*State Key Laboratory of Quantum Optics and Quantum Optics Devices, Institute of Laser Spectroscopy, Shanxi University, Taiyuan, Shanxi 030006, China. E-mail: chbqin@sxu.edu.cn, xlt@sxu.edu.cn; Tel: +86-351-7113863, +86-351-7018227*

[b]*Collaborative Innovation Center of Extreme Optics, Shanxi University, Taiyuan, Shanxi 030006, China*

[c]*Department of Physics, Shanxi Datong University, Datong, 037009, China*

†Electronic supplementary information (ESI) available. See DOI: 10.1039/d1nr00019e

The recent development in atomic-layered transition metal dichalcogenides (TMDs) with chemical formula MX_2 (such as MoS_2, $MoSe_2$, WS_2, and WSe_2) demonstrates that[21,22] TMDs are expected to be good candidates for spintronic technologies at room temperatures due to their giant intrinsic SOC.[20,23] The spin–orbit splittings in the TMD monolayer induced by spin–orbit interactions are several hundred milli-electron volts (meV) at the top of the valence band and a few to tens of meV for the bottom conduction band.[22,24] The origin of this dramatic interaction lies in the relatively heavy elements in the TMD materials and the involvement of the transition metal d orbitals.[25] Specifically, the valence band at the K point of the Brillouin zone is primarily composed of the $d_{x^2-y^2}$ and d_{xy} orbitals of the metal atom.[20,26] This giant splitting defines two different excitons attached to the two spin-split valence subbands, namely A and B excitons, respectively. On the other hand, the conduction band predominantly arises from the d_{z^2} orbital of the metal atom, and thus no significant splitting is expected. Nonetheless, a small spin splitting still survives after considering the role of less strongly coupled chalcogenide orbitals and the higher-order effect of the metal orbital.[27–29] Despite the giant splitting in the valence bands, engineering spin–orbit splitting is still strongly desired, which is an indispensable element of spintronics. Theoretical calculations have predicted that the spin–orbit splitting in the TMD monolayer can be effectively controlled *via* charge doping,[30] biaxial strain,[31,32] as well as co-doping of fluorine and group VA elements.[33] Very recently, spin–orbit engineering in $Mo_{(1-x)}W_xSe_2$ alloy monolayers has been experimentally demonstrated, in the view of the critical role of the transition metal d orbitals.[34]

Here, we experimentally demonstrated the engineering of the spin–orbit splitting of monolayer MoS_2 through laser irradiation under gas-controlled environments. We showed that the spin–orbit splitting, *i.e.*, the splitting between A and B excitons, can be enlarged from 152 meV of the as-prepared sample to 200 meV after irradiation with a 532 nm continuum-wave (CW) laser under inert gas atmospheres (including N_2 and He). The photoluminescence (PL) intensity of the B exciton has also been enhanced by more than two orders of magnitude in this stage. We further proved that the enhanced splitting could be reversibly reduced to 140 meV through laser irradiation under an air or O_2 atmosphere, associated with the recovery of the PL intensity of the B exciton. We attributed the reversible engineering of spin–orbit splitting and PL modulation to the enhanced absorption coefficient of monolayer MoS_2 and a subsequent increase of carrier concentrations, resulting in significant Auger recombination and pronounced band renormalization. This hypothesis has been confirmed by the reflectance contrast spectra during the engineering of spin–orbit interactions. Our approach provides new opportunities for reversible manipulation of SOC in monolayer TMDs after device fabrication at the desired locations, which has important implications in designing future spintronic devices.

2. Results

2.1. Reversible engineering of photoluminescence in monolayer MoS_2

For this study, monolayer MoS_2 was prepared by traditional chemical vapor deposition (CVD) on a Si/SiO_2 substrate (SixCarbon Technology, Shenzhen).[35] Fig. 1a presents the optical image of a typical sample. Isolated single-crystal MoS_2 flakes with a triangular shape and edge lengths ranging from 10 to 30 μm can be visualized. We have verified the thickness of these flakes to be a monolayer by atomic force microscopy (AFM), as presented in Fig. S1.† Almost uniform PL intensity (Fig. 1b) further confirms the high quality of the prepared sample. The corresponding PL spectra have been conducted with the excitation of a 532 nm CW laser (as the arrow shows in Fig. 1c). The spectral profile can be deconvoluted into two components, with energies of 1.824 eV and 1.976 eV, respectively. Straightforwardly, the two peaks can be attributed to the A and B excitons of monolayer MoS_2, with the spin–orbit splitting of 152 meV. The energy of excitons, the spin–orbit splitting, and the PL intensity ratio between A and B excitons are in good agreement with the relevant reports.[36–38]

The optical experiments, including laser irradiation and PL spectra measurements, were performed using a home-built scanning confocal microscope. The schematic diagram can be found in our previous works and the ESI (Fig. S2†).[39,40] Specifically, the prepared sample was placed on a motorized three-dimensional piezoelectric ceramic nano stage. As shown in Fig. S2,† the nano stage was covered by a polymethyl methacrylate (PMMA) chamber with a control vacuum valve on top of the plane. MoS_2 was engineered using a 532 nm CW laser *via* an objective (Nikon, 100×, NA 0.9), where PL was also collected using the same objective. All the experiments can be mainly divided into two cases. One is engineering monolayer MoS_2 with blowing N_2 gas (labeled as N_2). The other is irradiating the sample whilst blowing dry air (labeled as air).

Fig. 1d presents a typical PL trajectory of monolayer MoS_2 under laser irradiation against gas cycling. The irradiation and excitation of the MoS_2 sample are performed using a 532 nm CW laser with a power density of 21 MW cm^{-2}. For the pristine sample under air conditions, PL is slightly enhanced (roughly twice) under laser irradiation (Fig. S5†), which has been reported by our previous work and other groups.[39,41,42] This phenomenon can be understood as the formation of defects and adsorption of O_2/H_2O gas molecules, which will result in the depletion of free electrons and the conversion from charged exciton (X^T) to neutral exciton (X^A). Prolonged irradiation under air conditions will lead to crystal damage and PL quenching (Fig. S5†). However, further irradiation under a N_2 atmosphere shows an entirely new phenomenon, where PL can be significantly enhanced by orders of magnitude (from 16 kcps to 457 kcps) and can maintain the maximum PL without any quenching, as presented in Fig. 1d. Intriguingly, this enhanced PL can be reversed to the initial value in the air atmosphere by switching N_2 to air gas. In this case, PL will reduce rapidly and tend to reach a stable value in

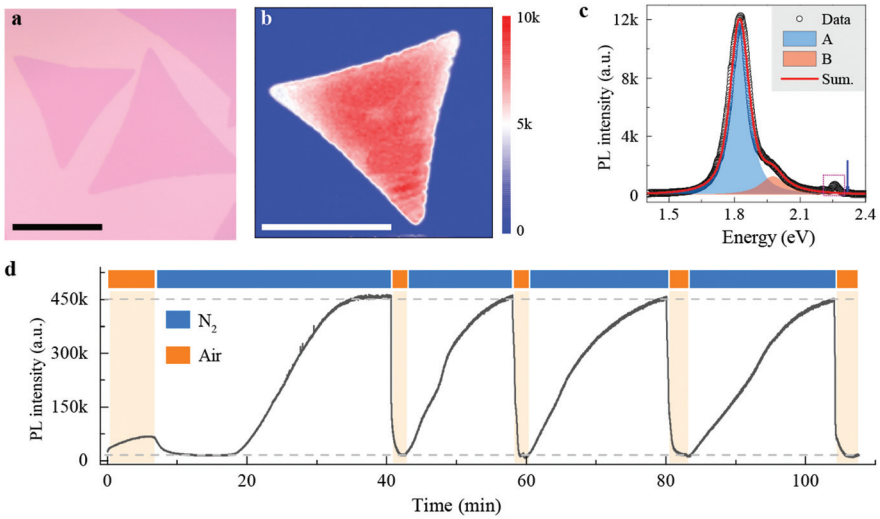

Fig. 1 Sample characterization and photoluminescence (PL) trajectory under controlled gas environments. (a) Optical image, (b) PL image, and (c) PL spectra of the prepared monolayer MoS_2. Scale bar in a and b: 20 μm. The spectral profile was deconvoluted using two Voigt functions. The weak peak highlighted by the dashed box is the Raman signal of monolayer MoS_2. (d) PL trajectory of monolayer MoS_2 under laser irradiation with controlled gas environments. The irradiation and excitation is performed using a 532 nm CW laser (denoted by the arrow in c). The power density was 21 MW cm^{-2}. Orange shades indicate PL behaviors under an air atmosphere, and blue shades indicate those under an N_2 atmosphere. Dashed lines are provided to guide the eye.

almost one minute. Even more intriguingly, this enhancement and reversal can be manipulated circularly merely by switching the N_2 and air atmospheres, as presented in Fig. 1d. At first glance, this reversible manipulation seems to be the result of the conversion between X^A and X^T.[39,41] However, the spectral analysis presents an entirely different conclusion.

2.2. Spectral analysis of the engineering processes

To reveal the underlying mechanism, the PL trajectory of the first circle is divided into four stages, highlighted by different colors, as shown in Fig. 2a. To explore the reversible process (PL quenching in an air atmosphere) more clearly, here we used a relatively low power density (3.5 MW cm^{-2}) to slow down the quenching process. PL spectra of the four stages have been empirically conducted, as presented in Fig. 2b–e, respectively. All the spectral profiles can be well deconvoluted into A and B excitons using Voigt functions (see Fig. S4† for detailed fitting curves). The determined photon energies, full width at half maximum (FWHM), integrated intensities, and the corresponding spectral weights for A and B excitons are presented in Fig. 2f–i, respectively (see Fig. S5† for a detailed comparison).

Now we provide a comprehensive description of the four stages. In stage I, PL of the A exciton is undoubtedly enhanced, which can be attributed to the conversion from X^T to X^A, as we discussed above and reported in the previous works.[39,41,42] We also find that the photon energy of the B exciton shows a slight redshift, which possibly originates from the formation of new defects and the reconstruction of the band structure. Next, in stage II, the FWHM of the B exciton dramatically broadens from 90 meV to 336 meV. That is to say, the same amount of the B exciton has been distributed into a broad energy region when blowing N_2. This unusual broadening of the FWHM will not further increase with prolonged irradiation times (as shown in stage III). On the other hand, the integrated PL abruptly quenched. From Fig. 2h, we can find that the PL intensity of the A exciton almost quenches to the background, while that of the B exciton presents slight enhancement. The conversion between A and B excitons can also be observed from their spectral weight variation, as shown in Fig. 2i. In stage III, we can find the PL intensity of the B exciton incredibly enhanced from 242 kcps to the maximum 25 191 kcps, corresponding to more than two orders of magnitude enhancement. Another distinguishing characteristic is that the FWHM of the B exciton has remained at around 320 meV (Fig. 2g), much broader than the initial value. Thus, PL spectra feature an extremely broad band. During this stage, the PL of the A exciton is also enlarged 3 times, with a remarkable redshift in its photon energy and broadening in the FWHM. After removing N_2, the photon energies, FWHM, and PL intensities of both A and B excitons will be restored to the beginning of stage III. The discontinuity of photon energy and FWHM between stages III and IV is probably due to the excitation power switching from 21 MW cm^{-2} to 3.5 MW cm^{-2}. In particular, we want to emphasize that all the PL evolutions (including peak energies, FWHM, PL intensity, and spectral weight) during stages III and IV can be well reproduced by further switching the atmosphere and laser irradiation. However, PL evolutions during stages I and II cannot be restored by switching the atmosphere, as shown in Fig. 1d. We have confirmed that these two stages (I and II) can be entirely removed by blowing N_2 onto the pristine sample for several

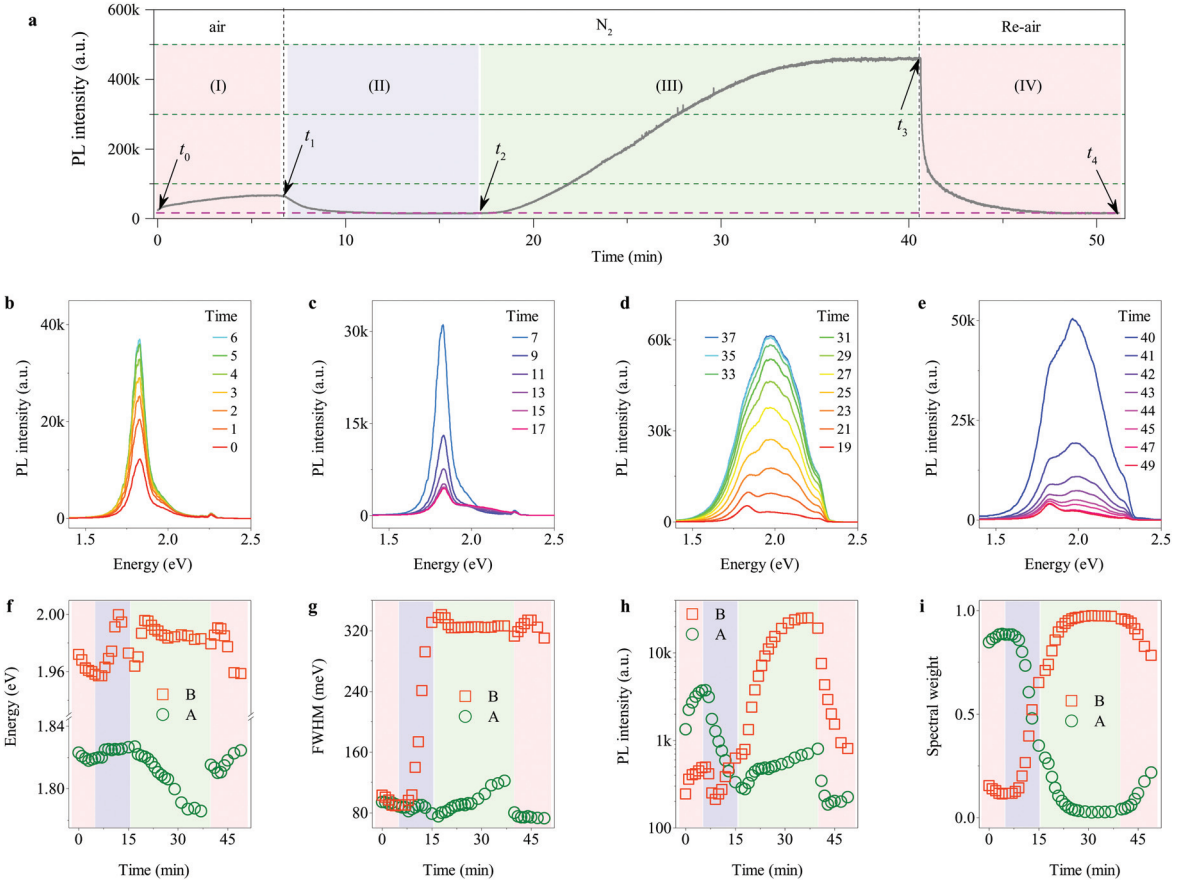

Fig. 2 PL evolution of monolayer MoS_2 during laser irradiation. (a) The PL trajectory is divided into four stages empirically. The laser power density was 21 MW cm^{-2} for stages I to III, and 3.5 MW cm^{-2} for stage IV. For the convenience of comparison, the PL intensity of stage IV has been magnified. For stages I and IV, MoS_2 was exposed to the air conditions. For stages II and III, MoS_2 was blown with an N_2 atmosphere. t_0 to t_4 are marked to illustrate the beginning and/or the end of each stage. Dashed lines are provided to guide the eye for comparing the PL intensities. (b)–(e) are the spectral profiles of the four stages. The integration time was 3 s; the interval between each spectrum was 1 minute. (f) Photon energies, (g) full width at half maxima (FWHM), (h) the integrated PL intensity, and (i) spectral weight of A and B excitons as the function of irradiation times. All the parameters are determined by deconvoluting the spectral profiles *via* Voigt functions.

minutes, rather than experimenting within the air atmosphere as a starting point (Fig. 4b, for example).

Beyond the variation of PL intensity and FWHM, the photon energy of the two excitons also shows dramatic changes. During stages III and IV, the A exciton presents a successive redshift from 1.826 eV to 1.785 eV (stage III) and then reverts to 1.825 eV (stage IV). On the other hand, the B exciton shows more complex behavior. Its photon energy shifts from 1.963 eV to 1.996 eV at the beginning of stage III and then continuously softens to 1.979 eV. In stage IV, the photon energy of the B exciton restores to 1.944 eV, as presented in Fig. 2f. The spin–orbit splitting can be determined by subtracting the photon energy of B from that of A, as shown in Fig. 3. We can find that the splitting increases from 140 meV (at the beginning of stage III) to 200 meV (at the end of stage III), and then recovers to close to 140 meV at the end of stage IV. As we expected, the spin–orbit splitting during stages III and IV can be reversibly engineered when we recurrently switch N_2 and air atmospheres. This phenomenon indicates that we can reversibly manipulate the spin–orbit splitting of monolayer MoS_2 as demanded by laser irradiation, through the switching of N_2 and air gases.

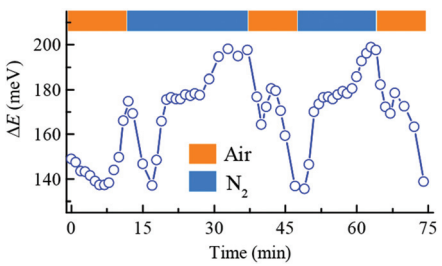

Fig. 3 Spin–orbit splitting of monolayer MoS_2 as a function of irradiation time during laser irradiation and switching of gases.

2.3. Reversible engineering under different conditions

To optimize engineering and demonstrate the robustness of this approach, we further perform systematic studies. Firstly,

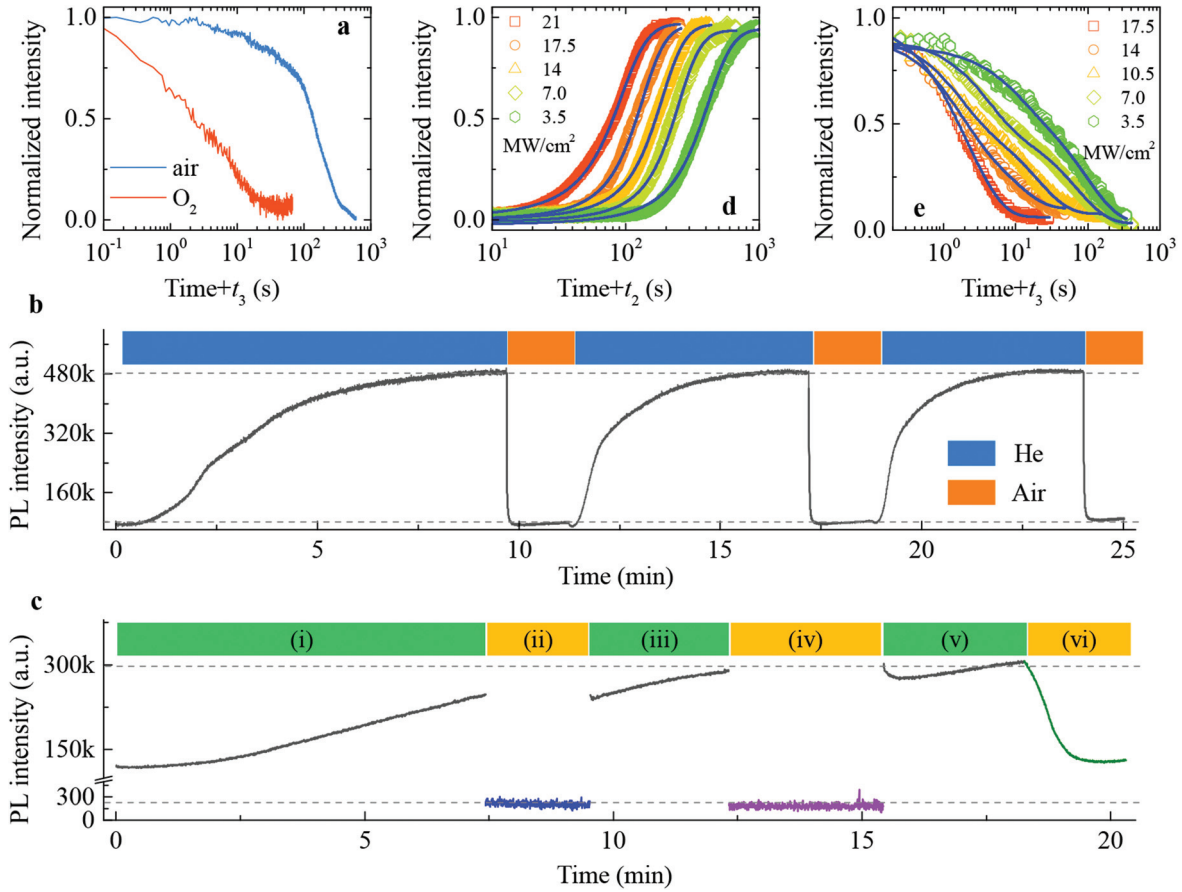

Fig. 4 PL evolution under different conditions. (a) PL trajectories under pure oxygen (O_2) and air conditions. The irradiation power density was 3.5 MW cm^{-2}. (b) PL trajectory of monolayer MoS_2 against gases cycling between He and air atmospheres. (c) PL trajectory of monolayer MoS_2 under different conditions. (i, iii and v) Both laser and N_2 are switched on. (ii) Switching off the laser but holding the N_2 atmosphere. (iv) Both laser and N_2 are switched off. (vi) Switching off the N_2 atmosphere but holding laser excitation. The irradiation power densities in b and c were both 21 MW cm^{-2}. (d) PL enhancement in a N_2 atmosphere, and (e) PL quenching in an air atmosphere under laser irradiation with different power densities, respectively. The solid lines in d and e are the fitting results obtained by the corresponding equations discussed in the main context.

we prove that oxygen (O_2) plays a vital role in the PL quenching process by changing the dry air to pure O_2, as shown in Fig. 4a. Note that PL quenches to the minimum value in hundreds of seconds (under 3.5 MW cm^{-2}) when blowing dry air gas. Yet, this process is almost one order of magnitude faster when blowing pure O_2 gas. This can be understood as the density of O_2 in pure oxygen atmospheres is five times that in the air atmosphere. We further verify that the reversible engineering of the spin–orbit splitting of monolayer MoS_2 and the corresponding PL enhancement can be achieved in other inert gases, such as helium (He) in Fig. 4b. PL evolution in He is similar to that in N_2 as well, as presented in Fig. S6.† It is worth mentioning that both PL enhancing and quenching under a He atmosphere are faster than those under a N_2 atmosphere. To exclude the thermal effect from the CW laser irradiation with high power density, we switch off the laser during the enhancing process under a N_2 atmosphere, as presented in Fig. 4c. Note that when we switch off the laser for several minutes (even several hours) and hold the N_2 atmosphere, the enhanced PL intensity still maintains when we switch on the laser again. If we switch off the laser and stop N_2 blowing, the PL shows a slight quenching and then shows the subsequent enhancement when N_2 blowing is restored. This slight quenching originates from the resident air when the laser is switched on. This result hints that the spin–orbit splitting engineering through our approach is robust and reliable. The modified splitting persists even without laser irradiation and a blowing N_2 atmosphere (Fig. 4c), manifesting great potential applications of monolayer MoS_2 in diverse spintronic and valleytronic devices.

The power-dependent PL evolutions are also performed to optimize the engineering processes. As illustrated in Fig. 4d and e, PL enhancement under a N_2 atmosphere and the subsequent PL quenching under air conditions at the laser power density ranging from 3.5 MW cm^{-2} to 21 MW cm^{-2} have been determined in our experiment. For both processes, the higher the power density, the faster the enhancing and quenching rates. We find that PL enhancement can be empirically fitted

using the formula, $I(t) = I_S + (I_0 - I_S)\cdot\{1 + \exp[(t - t_0)\gamma_\uparrow]\}^{-1}$, where I_S and I_0 denote the saturation and initial PL intensities, and $\gamma_\uparrow$ is the rate of the enhancement process. As shown by the solid lines in Fig. 4d, the fit results are in good agreement with experimental data. The determined $\gamma_\uparrow$ as a function of power density is presented in Fig. S7,† from which the acceleration of the enhancement process with the increase of power density can be determined. In contrast, PL quenching processes can be a good fit with a bi-exponential function $I(t) = I_0 + A_1\cdot e^{-t\cdot\gamma_1} + A_2\cdot e^{-t\cdot\gamma_2}$ (as presented by the solid lines in Fig. 4e). Fascinatingly, the averaged rate of the quenching process, $\gamma_\downarrow = (A_1\gamma_1 + A_2\gamma_2)/(A_1 + A_2)$, falls exponentially with the increase of laser power, as illustrated in Fig. S7.† Although the mechanisms behind the two empirical equations are under debate and further studies are needed, these parameters can still provide a guideline to precisely control the spin–orbit splitting and PL intensity of monolayer MoS_2.

3. Discussion

From spectral analysis and reversible engineering under different conditions, we can declare that the observed optical behaviors of monolayer MoS_2 are profoundly different from the phenomena reported in the previous works, where PL enhancing and quenching were mostly attributed to the conversion between X^T and X^A,[41,42] due to the formation of new defects and the depletion of free electrons.[43,44] Two main results support our conclusions. The first is that the engineering of both spin–orbit splitting and PL intensity is reversible, rather than the irreversible change for the formation of new defects.[39,40] The other is that the new-formed defects generally induce a new emission peak at the lower energy (~0.15 to 0.25 eV) of the A exciton.[45,46] However, no obvious PL peak was found in our experiments. To explore the reversible engineering of the spin–orbit splitting and the corresponding PL intensity, we propose a plausible scenario, as presented in Fig. 5. As we discussed above, the valence band (VB) will split into two subbands (A and B) due to the spin–orbit coupling. After laser excitation, electrons will populate at the lowest conduction band (CB), while holes occupy the highest valence band, resulting in the strong emission of the A exciton *via* radiative recombination, as shown in Fig. 5a. Generally, the radiative and non-radiative processes of excitons in monolayer MoS_2 can be expressed as $G = An + Bn^2 + Cn^3$, where G is the carrier generation/recombination rate;[47] n is the photoexcited carrier (electron/hole) concentration; A, B, and C represent the non-radiative Shockley–Read–Hall, radiative recombination, and Auger recombination coefficients, respectively. Here Auger recombination represents the annihilation of an exciton (an electron in the conduction band and a hole in the A subband) and an electron in the B subband, as shown in Fig. 5b. This phonon-assisted Auger recombination will result in the formation of holes in the B subband (Fig. 5c). The radiative recombination between the electrons in the conduction band and the holes in the B subband brings PL emission of the B exciton (Fig. 5d). From the equation, we can find that Auger recombination becomes dominant at high carrier concentrations. In other words, the higher the carrier concentrations, the stronger the emission of the B exciton. In our experiment, the excitation power density was maintained for each measurement, which is not responsible for the increase of carrier concentrations. Potential contributions from the laser-induced thermal effect have also been excluded by the PL evolution between switching on and off the laser irradiation (Fig. 4c).

Ultimately, we tentatively attribute the increase of carrier concentrations to the enhanced absorption coefficient of monolayer MoS_2 under the blowing of inert gases (N_2 and He). The enhanced coefficient probably results from the replacement of adsorbed O_2 by inert gases, where laser irradiation provides the activated energy to overcome the barrier of the replacement reactions. Considering that the quenching processes are much faster than the enhancing processes under laser irradiation with the same power density, we can speculate that the activated energy of the forward reaction (replacing O_2 with inert gases) is higher than that of the backward reaction (replacing inert gases by O_2). The elevated carrier densities not only enhance the Auger recombination but also result in a screened Coulomb interaction between charge carriers and possible dense electron–hole plasma.[48,49] According to the previous works,[25,50–52] this produces a pronounced many-particle renormalization effect, broadens the linewidth of resonant excitons, and reduces both the optical gap and exciton binding energies. The linewidth broadening is in agreement with our results, as shown in Fig. 2g. For the A exciton (X^A), the reduction of the optical gap is more pronounced. Hence the optical transition of the A exciton is a redshift, as we determined in Fig. 2f. Nevertheless, for the B exciton (X^B), we speculate that the reduction of binding energy is more significant (as shown in Fig. 5c), resulting in a blueshift of its photon energy. Consequently, the spin–orbit splitting in the conduction band (Δ_{SO}^{CB}) has been enlarged from a few meV to tens of meV. More importantly, it can be reversibly engineered as demanded by an all-optical procedure without an external electric field.

To prove our hypothesis, we further measured the reflectance contrast spectra during stages III and IV, respectively, as shown in Fig. 5e and f. Here $\Delta R/R = (R_{MoS_2} - R_{Si/SiO_2})/R_{Si/SiO_2}$, where R_{MoS_2} and R_{Si/SiO_2} are the reflected light intensity (see Methods). At the beginning of stage III, two peaks at around 1.88 eV and 2.01 eV can be determined in the reflectance contrast spectra, coinciding with the absorption of A and B excitons reported in the relevant works.[36] With an increase of laser irradiation under a N_2 atmosphere, the enhancement and broadening of reflectance spectra can be demonstrated, indicating the validity of our hypothesis. The full recovery of the reflectance contrast spectra in stage IV (Fig. 5f) further supports our conclusions.

Although a plausible mechanism has been proposed, further experiments are still needed to clarify the crucial roles of O_2 and inert gases, as well as Auger recombination. Firstly,

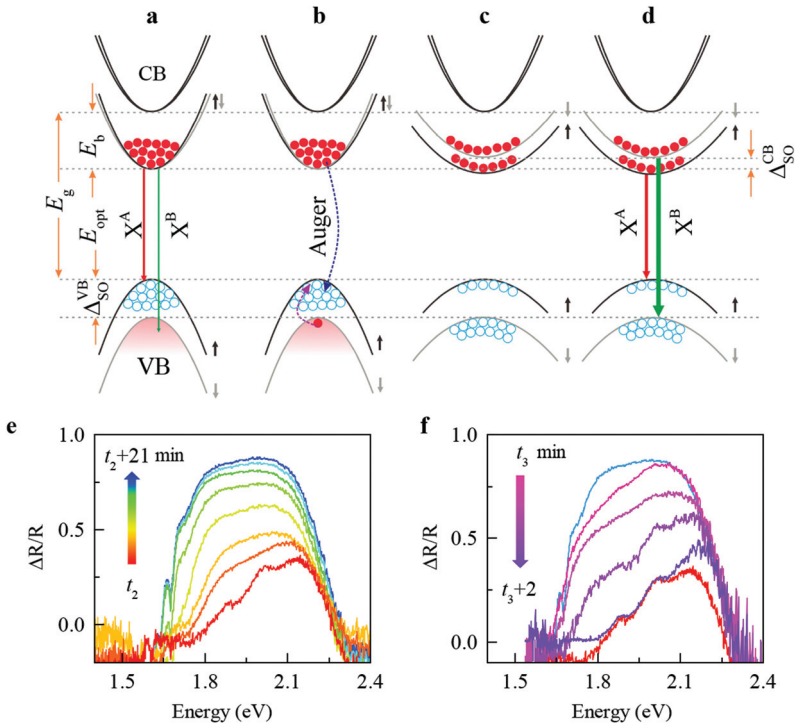

Fig. 5 Schematic illustration of spin–orbit splitting engineering in monolayer MoS_2. Filled (red) and empty (blue) circles indicate the electrons and holes. CB (VB) represents the conduction band (valence band). The spin-up (spin-down) subbands are denoted by the arrows in black (gray) colors. E_g, E_{opt}, and E_b represent the electronic bandgap, optical bandgap, and the binding energy of excitons, respectively. Δ_{SO}^{VB} and Δ_{SO}^{CB} indicate the corresponding spin–orbit splitting of the VB and CB. (a) At low carrier concentrations, the radiative recombination of electrons and holes leads to the PL emission of the A exciton (X^A). (b) At high carrier concentrations, Auger recombination becomes dominant, which will annihilate two electrons (one in CB, one in B sub-bands) and a hole (in A sub-band) using a non-radiative process. (c) Auger recombination results in the population of holes in the B subband, and subsequent band renormalizations. (d) The radiative recombination of electrons and holes in the B sub-band leads to the PL emission of the B exciton. Evolution of reflectance contrast spectra during stage III (e) and stage IV (f) processes shown in Fig. 2. t_2 and t_3 denote the beginning of the two approaches, as marked in Fig. 2a. The time intervals for e and f are 3 min and 20 s, respectively. The highest and lowest curves in F are the end and beginning reflectance spectra in stage III (in e).

comprehensive calculations, taking carrier density and Auger recombination into account, should be performed to reveal the role of inert gases and O_2 in the photoexcited carriers as well as the spin–orbit splitting associated with the variation of carrier density. Secondly, crystal inversion symmetry breaking together with strong SOC leads to coupled spin and valley in the TMD monolayer.[53] Reversible engineering of spin–orbit splitting offers opportunities for the control of spin and valley in these materials, providing a new route to design high-performance monolayer TMD-based valleytronics and opto-valleytronics. Furthermore, this coupling results in an energy separation between the spin-allowed and optically active transitions, as well as the spin-forbidden and optically inactive transitions, namely bright and dark excitons.[54–56] The engineering of spin–orbit splitting changes the carrier populations between the two transitions, and thus new evidence and novel physics may be determined by further experiments. Last but not least, the kinetics of the replacement reaction typically depends upon temperature and the concentration of reactants. Thus, the enhancing and quenching processes may be controlled by changing the temperature of monolayer MoS_2, as well as the concentrations of O_2, N_2, or He. In particular, the temperature-dependent PL spectra manifest abundant information involving the increase of the FWHM and the exciton–phonon scattering (Auger recombination).

4. Conclusion

In conclusion, we have reversibly engineered spin–orbit splitting and PL emission of the B exciton in monolayer MoS_2 by laser irradiation under controlled gas environments (switching between inert gases, such as N_2 and He, and air atmosphere). PL spectra evolutions during the reversible manipulation and power-dependent PL behaviors have been conducted and analyzed. The spin–orbit splitting is modified between 140 meV and 200 meV. The PL intensity of the B exciton has been enhanced by two orders of magnitude. We also show that the reversible and controllable PL spectral features enable explorations of versatile optical applications, such as optical recording (Fig. S8†). After excluding the thermal effect originating from the CW laser irradiation with high power, we propose a plausible mechanism to explore this unique PL feature, where the emission of the B exciton is attributed to the photon-assisted

Auger recombination. We suggest that Auger recombination can be modified during the replacement reactions between inert and air gases. However, the underlying physics remains elusive and needs further studies.

5. Experimental section

5.1. Optical measurements

A schematic of the experimental setup is presented in Fig. S2.† A home-built scanning confocal system based on an invert microscope (Nikon, TE2000-U) was used to engineer monolayer MoS_2 and take PL spectroscopy by utilizing a 532 nm CW laser (MSL-III-532, Changchun New Industries Optoelectronics Tech. Co., Ltd). After being extended using a beam expander and filtered using an excitation filter (LL01-532-25, Semrock), the laser was directed using a dichroic mirror (Di01-RE532, Semrock) towards a dry objective (100×, NA 0.9, Nikon) to engineer and excite the monolayer MoS_2, which was placed on a motorized three-dimensional piezoelectric ceramic nano stage (200/20SG, Tritor). The laser spot diameter was around 1 μm. PL from MoS_2 was collected using the same objective and passed through a dichroic mirror and a notch filter (NF03-532E-25, Semrock). Then, PL was split into two beams using a beam splitter with a ratio of 7 to 3. The weaker one was further filtered spatially using a 100 μm spatial filter and an emission filter (LP03-532RE-25, Semrock) to block the back-scattered laser light. PL intensity was detected using a single photon detector (SPCM-AQR-15, PerkinElmer). The stronger beam was sent through a monochromator with a focal length of 30 cm, equipped with a charge-coupled device (DR-316B-LDC, Andor). Monolayer MoS_2 was covered by a polymethyl methacrylate (PMMA) chamber with a control vacuum valve on top of the plane (Fig. S3†). Dry air, N_2, He, and O_2 with a controlled flow rate were used to blow the sample. All the experiments were performed at room temperature. For the reflectance contrast measurements, a broadband light (DH-2000-BAL, Ocean Optics) was focused onto the sample using the same objective.

Author contributions

C. Q. and L. X. designed and supervised the experiments. X. L., S. H., and Y. G. carried out the optical experiments. G. Z., R. C., and J. H. prepared and characterized the sample. S. J. was responsible for gas management. X. L., C. Q., Y. G., and X. L. wrote the manuscript. All authors commented on the manuscript.

Data availability

The data that support the findings of this study are available from the corresponding author upon reasonable request.

Conflicts of interest

The authors declare that there are no competing interests.

Acknowledgements

The authors gratefully acknowledge support from the National Key Research and Development Program of China (grant no. 2017YFA0304203), the National Natural Science Foundation of China (no. 91950109, 61875109, 62075120, 62075122, and 62011530047), the Natural Science Foundation of Shanxi Province (no. 201901D111010(ZD)), PCSIRT (no. IRT_17R70), 111 projects (grant no. D18001), 1331KSC, and PTIT.

References

1 A. Soumyanarayanan, N. Reyren, A. Fert and C. Panagopoulos, Emergent phenomena induced by spin-orbit coupling at surfaces and interfaces, *Nature*, 2016, **539**(7630), 509.
2 M. Smidman, M. B. Salamon, H. Q. Yuan and D. F. Agterberg, Superconductivity and spin-orbit coupling in non-centrosymmetric materials: a review, *Rep. Prog. Phys.*, 2017, **80**(3), 036501.
3 A. Manchon, H. C. Koo, J. Nitta, S. M. Frolov and R. A. Duine, New perspectives for Rashba spin-orbit coupling, *Nat. Mater.*, 2015, **14**(9), 871.
4 Y. J. Lin, K. Jimenez-Garcia and I. B. Spielman, Spin-orbit-coupled Bose-Einstein condensates, *Nature*, 2011, **471**(7336), 83.
5 Y. K. Kato, R. C. Myers, A. C. Gossard and D. D. Awschalom, Observation of the spin Hall effect in semiconductors, *Science*, 2004, **306**(5703), 1910.
6 D. Sun, K. J. van Schooten, M. Kavand, H. Malissa, C. Zhang, M. Groesbeck, C. Boehme and Z. V. Vardeny, Inverse spin Hall effect from pulsed spin current in organic semiconductors with tunable spin-orbit coupling, *Nat. Mater.*, 2016, **15**(8), 863.
7 M. Z. Hasan and C. L. Kane, Colloquium: Topological insulators, *Rev. Mod. Phys.*, 2010, **82**(4), 3045.
8 Y. Fan, P. Upadhyaya, X. Kou, M. Lang, S. Takei, Z. Wang, J. Tang, L. He, L. T. Chang, M. Montazeri, *et al.*, Magnetization switching through giant spin-orbit torque in a magnetically doped topological insulator heterostructure, *Nat. Mater.*, 2014, **13**(7), 699.
9 M. M. Desjardins, L. C. Contamin, M. R. Delbecq, M. C. Dartiailh, L. E. Bruhat, T. Cubaynes, J. J. Viennot, F. Mallet, S. Rohart, A. Thiaville, *et al.*, Synthetic spin-orbit interaction for Majorana devices, *Nat. Mater.*, 2019, **18**(10), 1060.
10 A. A. Burkov and L. Balents, Weyl semimetal in a topological insulator multilayer, *Phys. Rev. Lett.*, 2011, **107**(12), 127205.

11 V. Baltz, A. Manchon, M. Tsoi, T. Moriyama, T. Ono and Y. Tserkovnyak, Antiferromagnetic spintronics, *Rev. Mod. Phys.*, 2018, **90**(1), 015005.
12 W. Han, R. K. Kawakami, M. Gmitra and J. Fabian, Graphene spintronics, *Nat. Nanotechnol.*, 2014, **9**(10), 794.
13 K. Premasiri, S. K. Radha, S. Sucharitakul, U. R. Kumar, R. Sankar, F.-C. Chou, Y.-T. Chen and X. P. A. Gao, Tuning Rashba Spin–Orbit Coupling in Gated Multilayer InSe, *Nano Lett.*, 2018, **18**(7), 4403.
14 K. Premasiri and X. P. A. Gao, Tuning spin-orbit coupling in 2D materials for spintronics: a topical review, *J. Phys.: Condens. Matter*, 2019, **31**(19), 193001.
15 M. P. Nowak, B. Szafran, F. M. Peeters, B. Partoens and W. J. Pasek, Tuning of the spin-orbit interaction in a quantum dot by an in-plane magnetic field, *Phys. Rev. B: Condens. Matter Mater. Phys.*, 2011, **83**(24), 245324.
16 A. Sasaki, S. Nonaka, Y. Kunihashi, M. Kohda, T. Bauernfeind, T. Dollinger, K. Richter and J. Nitta, Direct determination of spin-orbit interaction coefficients and realization of the persistent spin helix symmetry, *Nat. Nanotechnol.*, 2014, **9**(9), 703.
17 L. Huang, Z. Meng, P. Wang, P. Peng, S.-L. Zhang, L. Chen, D. Li, Q. Zhou and J. Zhang, Experimental realization of two-dimensional synthetic spin–orbit coupling in ultracold Fermi gases, *Nat. Phys.*, 2016, **12**(6), 540.
18 G. Herranz, G. Singh, N. Bergeal, A. Jouan, J. Lesueur, J. Gazquez, M. Varela, M. Scigaj, N. Dix, F. Sanchez, *et al.*, Engineering two-dimensional superconductivity and Rashba spin-orbit coupling in $LaAlO_3/SrTiO_3$ quantum wells by selective orbital occupancy, *Nat. Commun.*, 2015, **6**, 6028.
19 S. Nadj-Perge, S. M. Frolov, E. P. Bakkers and L. P. Kouwenhoven, Spin-orbit qubit in a semiconductor nanowire, *Nature*, 2010, **468**(7327), 1084.
20 Z. Y. Zhu, Y. C. Cheng and U. Schwingenschlögl, Giant spin-orbit-induced spin splitting in two-dimensional transition-metal dichalcogenide semiconductors, *Phys. Rev. B: Condens. Matter Mater. Phys.*, 2011, **84**(15), 153402.
21 M. Chhowalla, H. S. Shin, G. Eda, L. J. Li, K. P. Loh and H. Zhang, The chemistry of two-dimensional layered transition metal dichalcogenide nanosheets, *Nat. Chem.*, 2013, **5**(4), 263.
22 X. Xu, W. Yao, D. Xiao and T. F. Heinz, Spin and pseudospins in layered transition metal dichalcogenides, *Nat. Phys.*, 2014, **10**(5), 343.
23 B. T. Zhou, K. Taguchi, Y. Kawaguchi, Y. Tanaka and K. T. Law, Spin-orbit coupling induced valley Hall effects in transition-metal dichalcogenides, *Commun. Phys.*, 2019, **2**(1), 26.
24 A. Delhomme, G. Butseraen, B. Zheng, L. Marty, V. Bouchiat, M. R. Molas, A. Pan, K. Watanabe, T. Taniguchi, A. Ouerghi, *et al.*, Magneto-spectroscopy of exciton Rydberg states in a CVD grown WSe_2 monolayer, *Appl. Phys. Lett.*, 2019, **114**(23), 232104.
25 G. Wang, A. Chernikov, M. M. Glazov, T. F. Heinz, X. Marie, T. Amand and B. Urbaszek, Colloquium: Excitons in atomically thin transition metal dichalcogenides, *Rev. Mod. Phys.*, 2018, **90**(2), 021001.
26 H. Braganca, F. Riche, F. Qu, V. Lopez-Richard and G. E. Marques, Dark-exciton valley dynamics in transition metal dichalcogenide alloy monolayers, *Sci. Rep.*, 2019, **9**(1), 4575.
27 K. Marinov, A. Avsar, K. Watanabe, T. Taniguchi and A. Kis, Resolving the spin splitting in the conduction band of monolayer MoS_2, *Nat. Commun.*, 2017, **8**(1), 1938.
28 K. Kosmider, J. W. Gonzalez and J. Fernandez-Rossier, Large spin splitting in the conduction band of transition metal dichalcogenide monolayers, *Phys. Rev. B: Condens. Matter Mater. Phys.*, 2013, **88**(24), 245436.
29 Y. Liu, K. Tom, X. Zhang, S. Lou, Y. Liu and J. Yao, Alloying effect on bright–dark exciton states in ternary monolayer Mo_xW_{1-x},Se_2, *New J. Phys.*, 2017, **19**(7), 073018.
30 J. Chen, K. Wu, H. Ma, W. Hu and J. Yang, Tunable Rashba spin splitting in Janus transition-metal dichalcogenide monolayers via charge doping, *RSC Adv.*, 2020, **10**(11), 6388.
31 M. A. U. Absor, I. Santoso, A. K. Harsojo, H. Kotaka, F. Ishii and M. Saito, Polarity tuning of spin-orbit-induced spin splitting in two-dimensional transition metal dichalcogenides, *J. Appl. Phys.*, 2017, **122**(15), 153905.
32 M. A. U. Absor, H. Kotaka, F. Ishii and M. Saito, Strain-controlled spin splitting in the conduction band of monolayer WS_2, *Phys. Rev. B*, 2016, **94**(11), 115131.
33 S. Guo, H. Zheng, Y. Wang and J. Zhang, Achieving giant spin-orbit splitting in conduction band of monolayer WS_2 *via n-p* co-doping, *AIP Adv.*, 2019, **9**(7), 075304.
34 G. Wang, C. Robert, A. Suslu, B. Chen, S. Yang, S. Alamdari, I. C. Gerber, T. Amand, X. Marie, S. Tongay, *et al.*, Spin-orbit engineering in transition metal dichalcogenide alloy monolayers, *Nat. Commun.*, 2015, **6**, 10110.
35 D. Zhou, H. Shu, C. Hu, L. Jiang, P. Liang and X. Chen, Unveiling the Growth Mechanism of MoS_2 with Chemical Vapor Deposition: From 2D Planar Nucleation to Self-Seeding Nucleation, *Cryst. Growth Des.*, 2018, **18**, 1012.
36 K. P. Dhakal, D. L. Duong, J. Lee, H. Nam, M. Kim, M. Kan, Y. H. Lee and J. Kim, Confocal absorption spectral imaging of MoS_2: optical transitions depending on the atomic thickness of intrinsic and chemically doped MoS_2, *Nanoscale*, 2014, **6**(21), 13028.
37 J. G. Kim, W. S. Yun, S. Jo, J. Lee and C. H. Cho, Effect of interlayer interactions on exciton luminescence in atomic-layered MoS_2 crystals, *Sci. Rep.*, 2016, **6**, 29813.
38 Y. Jung, J. Shen and J. J. Cha, Surface effects on electronic transport of 2D chalcogenide thin films and nanostructures, *Nano Convergence*, 2014, **1**(1), 18.
39 C. Qin, Y. Gao, L. Zhang, X. Liang, W. He, G. Zhang, R. Chen, J. Hu, L. Xiao and S. Jia, Flexible engineering of light emission in monolayer MoS_2 *via* direct laser writing for multimode optical recording, *AIP Adv.*, 2020, **10**(4), 045230.
40 C. B. Qin, X. L. Liang, S. P. Han, G. F. Zhang, R. Y. Chen, J. Y. Hu, L. T. Xiao and S. T. Jia, Giant enhancement of

photoluminescence emission in monolayer WS_2 by femtosecond laser irradiation, *Front. Phys.*, 2020, **16**(1), 12501.

41 H. M. Oh, G. H. Han, H. Kim, J. J. Bae, M. S. Jeong and Y. H. Lee, Photochemical Reaction in Monolayer MoS_2 via Correlated Photoluminescence, Raman Spectroscopy, and Atomic Force Microscopy, *ACS Nano*, 2016, **10**(5), 5230.

42 H. Ardekani, R. Younts, Y. Yu, L. Cao and K. Gundogdu, Reversible Photoluminescence Tuning by Defect Passivation via Laser Irradiation on Aged Monolayer MoS_2, *ACS Appl. Mater. Interfaces*, 2019, **11**(41), 38240.

43 P. K. Chow, R. B. Jacobs-Gedrim, J. Gao, T. M. Lu, B. Yu, H. Terrones and N. Koratkar, Defect-Induced Photoluminescence in Monolayer Semiconducting Transition Metal Dichalcogenides, *ACS Nano*, 2015, **9**(2), 152.

44 H. Y. Nan, Z. L. Wang, W. H. Wang, Z. Liang, Y. Lu, Q. Chen, D. W. He, P. H. Tan, F. Miao, X. R. Wang, *et al.*, Strong Photoluminescence Enhancement of MoS_2 through Defect Engineering and Oxygen Bonding, *ACS Nano*, 2014, **8**(6), 5738.

45 S. Tongay, J. Zhou, C. Ataca, J. Liu, J. S. Kang, T. S. Matthews, L. You, J. Li, J. C. Grossman and J. Wu, Broad-Range Modulation of Light Emission in Two-Dimensional Semiconductors by Molecular Physisorption Gating, *Nano Lett.*, 2013, **13**(6), 2831.

46 S. Mouri, Y. Miyauchi and K. Matsuda, Tunable Photoluminescence of Monolayer MoS_2 via Chemical Doping, *Nano Lett.*, 2013, **13**(12), 5944.

47 O. Salehzadeh, N. H. Tran, X. Liu, I. Shih and Z. Mi, Exciton kinetics, quantum efficiency, and efficiency droop of monolayer MoS_2 light-emitting devices, *Nano Lett.*, 2014, **14**(7), 4125.

48 A. Steinhoff, J. H. Kim, F. Jahnke, M. Rosner, D. S. Kim, C. Lee, G. H. Han, M. S. Jeong, T. O. Wehling and C. Gies, Efficient Excitonic Photoluminescence in Direct and Indirect Band Gap Monolayer MoS_2, *Nano Lett.*, 2015, **15**(10), 6841.

49 Y. Yu, A. W. Bataller, R. Younts, Y. Yu, G. Li, A. A. Puretzky, D. B. Geohegan, K. Gundogdu and L. Cao, Room-Temperature Electron-Hole Liquid in Monolayer MoS_2, *ACS Nano*, 2019, **13**(9), 10351.

50 D. Erben, A. Steinhoff, C. Gies, G. Schönhoff, T. O. Wehling and F. Jahnke, Excitation-induced transition to indirect band gaps in atomically thin transition-metal dichalcogenide semiconductors, *Phys. Rev. B*, 2018, **98**(3), 035434.

51 M. Koperski, M. R. Molas, A. Arora, K. Nogajewski, A. O. Slobodeniuk, C. Faugeras and M. Potemski, Optical properties of atomically thin transition metal dichalcogenides: observations and puzzles, *Nanophotonics*, 2017, **6**(6), 1289.

52 D. L. Duong, S. J. Yun and Y. H. Lee, van der Waals Layered Materials: Opportunities and Challenges, *ACS Nano*, 2017, **11**(12), 11803.

53 D. Xiao, G.-B. Liu, W. Feng, X. Xu and W. Yao, Coupled Spin and Valley Physics in Monolayers of MoS_2 and Other Group-VI Dichalcogenides, *Phys. Rev. Lett.*, 2012, **108**(19), 196802.

54 Y. Zhou, G. Scuri, D. S. Wild, A. A. High, A. Dibos, L. A. Jauregui, C. Shu, K. De Greve, K. Pistunova, A. Y. Joe, *et al.*, Probing dark excitons in atomically thin semiconductors via near-field coupling to surface plasmon polaritons, *Nat. Nanotechnol.*, 2017, **12**(9), 856.

55 M. R. Molas, C. Faugeras, A. O. Slobodeniuk, K. Nogajewski, M. Bartos, D. M. Basko and M. Potemski, Brightening of dark excitons in monolayers of semiconducting transition metal dichalcogenides, *2D Mater.*, 2017, **4**(2), 021003.

56 X. X. Zhang, T. Cao, Z. Lu, Y. C. Lin, F. Zhang, Y. Wang, Z. Li, J. C. Hone, J. A. Robinson, D. Smirnov, *et al.*, Magnetic brightening and control of dark excitons in monolayer WSe_2, *Nat. Nanotechnol.*, 2017, **12**(9), 883.